ACS Catalysis

pubs.acs.org/acscatalysis

Research Article

Unraveling Enhanced Activity, Selectivity, and Coke Resistance of Pt−Ni Bimetallic Clusters in Dry Reforming

Juntian Niu, Yalan Wang, Shirley E. Liland, Samuel K. Regli, Jia Yang, Kumar R. Rout, Jun Luo, Magnus Rønning, Jingyu Ran, and De Chen*

Cite This: *ACS Catal.* 2021, 11, 2398−2411

Read Online

ACCESS | Metrics & More | Article Recommendations | Supporting Information

ABSTRACT: By introducing Pt atoms into the surface of reduced hydrotalcite (HT)-derived nickel (Ni/HT) catalysts by redox reaction, we synthesized an enhanced active and stable Ni-based catalyst for methane dry reforming reaction. The bimetallic Pt−Ni catalysts can simultaneously enhance the catalyst activity, increase the H_2/CO ratio by suppressing reverse water−gas shift reaction, and enhance the stability by increasing the resistance to the carbon deposition during the reaction. Kinetic study showed that 1.0Pt−12Ni reduces the activation energy for CH_4 dissociation and enhances the catalytic activity of the catalyst and lowers the energy barrier for CO_2 activation and promotes the formation of surface O* by CO_2 adsorptive dissociation. It is beneficial to enhance the resistance to the carbon deposition and prolong its service life in the reaction process. In addition, density-functional theory calculations rationalized the higher coke resistance of Pt−Ni catalysts where CH is more favorable to be oxidized instead of cracking into surface carbon on the Pt−Ni surface, compared with Ni(111) and Pt(111). Even if a small amount of carbon deposited on the Pt−Ni surface, its oxidation process requires a lower activation barrier. Thus, it demonstrates that the bimetallic Pt−Ni catalyst has the best ability to resist carbon deposition compared with monometallic samples.

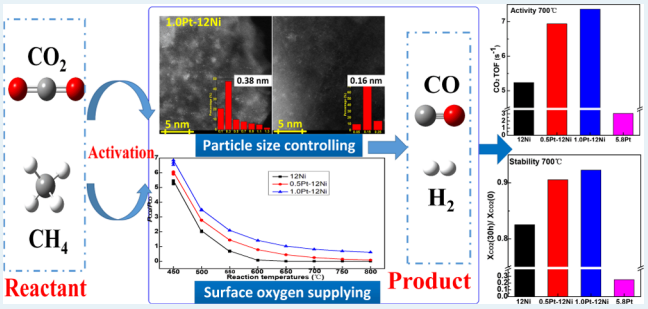

KEYWORDS: *methane dry reforming, coke resistance, surface oxygen, Pt−Ni cluster catalysts, DFT*

1. INTRODUCTION

Dry reforming of methane (DRM) provides a feasible way to reduce greenhouse gases of CH_4 and CO_2 and convert them into synthesis gas (H_2 and CO), one of the most important intermediates for producing liquid fuels and synthesizing high-value chemicals.[1−7] In addition, DRM reaction is regarded as a promising alternative for the steam reforming of methane since it can directly utilize raw natural gas[8] and the produced syngas possessing a lower H_2/CO ratio.[9−11] Ni-based catalysts are seen as an attractive candidate for the DRM process because of their low cost and high activity.[12,13] However, methane dry reforming is inevitably accompanied by the deactivation of catalysts due to the coke formation, metal oxidation, and particle sintering.[14] Besides, the occurrence of the reverse water−gas shift reaction (RWGS: $H_2 + CO_2 \rightarrow CO + H_2O$) would cause an undesired H_2/CO ratio lower than 1.[15] Although Ni is still the most often used catalyst, promoters or alloying with second metals is normally required to achieve the high activity, selectivity, and stability of DRM, simultaneously.[16]

Bimetallic catalysts have received increasing attention in recent years, and they could tune the electronic and chemical properties from monometallic ones, thus providing an opportunity to design new catalysts with improved activity, selectivity, and stability.[17−19] Ni is also the most widely used element in the transition metal-based catalysts and has an excellent ability to form bimetallic systems with other metals.[20−22] Therefore, noble metals such as Pt could be applied to promote the Ni catalysts to enhance their catalytic performance in DRM.[23]

Ni−noble metal bimetallic catalysts have been explored experimentally in methane dry reforming. It has been reported that addition of a certain amount of noble metals such as Pt could promote the reducibility of Ni[24] and reduce the metal crystal size compared to that in monometallic Pt and Ni catalysts.[25] Pt−Ni bimetals can efficiently enhance the resistance against coke formation in the DRM process[24−30] but generally reduced the activity compared to Ni catalysts.[24−26] In contrast, a higher activity of bimetallic Pt−Ni/Al_2O_3 was also reported.[29] Another challenge for dry reforming is the much lower H_2/CO ratio (typically lower

Received: October 13, 2020
Revised: December 28, 2020
Published: February 8, 2021

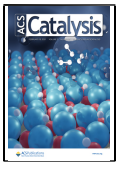

https://dx.doi.org/10.1021/acscatal.0c04429
ACS Catal. 2021, 11, 2398−2411

than 0.8[24−26]) generated than the stoichiometric one of 1 due to the reverse water−gas shift reaction. The challenge also remains in the Pt−Ni bimetallic catalyst. It is highly desired to develop new catalysts to achieve the high activity, high selectivity, and good stability simultaneously through rationally designing and manipulating the surface reactions. A better understanding of the surface reaction mechanism on Pt−Ni bimetals and unrevealing the effect of Pt in the bimetal on activity, selectivity, and stability are essential for the purpose.

There have been density-functional theory (DFT) calculations performed to validate the experimental observations or to give fundamental in-depth insights,[31,32] in particular for the coke resistance of dry reforming catalysts. Most of the work has been focused only on C−H activation of the methane on bimetallic catalysts. Bimetallic catalysts provide a unique way to tune the C−H bond activation of methane.[21,22,33] An increase in the methane activation barrier has been rationalized to the observed better coke resistance of Pt−Ni catalysts.[21,22] However, there are two general strategies for enhancing carbon formation resistance by reducing the surface carbon (C*) concentration, namely, lowering the C−H bond and strengthening the C* removal by surface oxidation of OH*/O*. A more systematic study is highly desired to understand better the effect of Pt−Ni bimetals on the surface reactions in DMR.

In this paper, we focus on unraveling the role of Pt in the activity, selectivity, and stability of the Pt−Ni catalysts in methane dry reforming by a combined experimental and theoretic approach. Besides, we report a three birds, one stone strategy for Pt−Ni bimetallic clusters to simultaneously achieve the high activity, better stability, and high selectivity to hydrogen to get an H_2/CO ratio close to 1. We synthesized well-dispersed Pt−Ni clusters from the surface redox reactions of a Ni catalyst, supported on oxides generated from double-layered hydroxides.[34,35] Herein, we propose a reaction mechanism that Pt−Ni enhanced the stability and H_2/CO ratio and activity compared to monometallic Ni and Pt catalysts by combined kinetic study and DFT simulations.

2. EXPERIMENTAL AND THEORETICAL METHODS

2.1. Catalyst Preparation. Monometallic 12 wt % Ni (name as 12Ni) derived from a hydrotalcite-like precursor[4,19,36−38] has been prepared by co-precipitation using a metal nitrite component, keeping the ratio of Ni/Mg/Al at 0.37:2.63:1. An aqueous solution of NaOH and Na_2CO_3 (400 mL) was added at a constant rate into a reactor containing an aqueous solution of nitrates Ni^{2+}, Mg^{2+}, and Al^{3+} (400 mL) in a period of 2 h. After the addition was finished, the pH of the mixture solution was kept around 9. Then, the reactor containing the mixture solution was kept in an oil bath for 16 h at 80 °C. The resultant hydrotalcite was cooled, then filtered, and washed with deionized water several times. The hydrotalcite was then dried at 100 °C for 12 h (denoted as NiO/HT). The prepared catalyst was confirmed to have typical hydrotalcite structures by XRD analysis. Subsequently, the catalyst was calcined in the air at 600 °C for 6 h, which destroyed the hydrotalcite structure and formed mixed oxides NiO/Mg(Al)O, marked as 12Ni. In addition, for the 5.8 wt % Pt/HT catalyst synthesis, we prepared the Mg−Al hydrotalcite first. Then, after the calcination of the Mg−Al hydrotalcite at 600 °C for 6 h, we impregnated the Pt precursor into a Mg(Al)O support, marked as 5.8Pt. All the catalysts were crushed into powder and sieved to a particle size of 53−125 μm.

The monometallic Ni catalyst was reduced in the mixture gas H_2 (50 mL/min) and Ar (50 mL/min) at 670 °C for 16 h to convert NiO into metallic Ni. The reduced Ni catalyst was kept in inert gas Ar to avoid re-oxidation. Pt−Ni bimetallic catalysts were prepared by redox reaction of the reduced Ni catalyst with the Pt ions in the form of a precursor salt at ambient temperature. The amount of the Pt precursor $[Pt(NH_4)_3(NO_3)_2]$ was determined based on the weight of Pt loading, 0.5 wt % Pt and 1.0 wt % Pt. During the redox reaction, the salt solution was circulated into the Ni catalysts placed in a fixed bed reactor over 10 h, where Ni atoms were gradually substituted into Pt atoms on the surface of Ni particles and Ni^{2+} formed accordingly, $Pt^{2+} + Ni \rightarrow Pt + Ni^{2+}$. After the reaction, the catalysts were passivated in 1vol % O_2/Ar for 1 h and then filtrated and washed several times to remove formed Ni^{2+} and unreacted Pt^{2+}, followed by drying in air at 100 °C for 12 h. Finally, the Pt−Ni catalysts were re-calcined in air at 600 °C for 6 h and named as 0.5Pt−12Ni and 1.0Pt−12Ni. All the catalysts were crushed into powder and sieved to a particle size of 53−125 μm.

The detailed information of the instrument type and reaction conditions for Ni, Pt, and Pt−Ni catalyst characterizations is provided in the Supporting Information.

2.2. Catalytic Tests. The catalytic test was performed at 1 atm in a fixed bed tubular reactor of quartz with an internal diameter of 10 mm, and a K-type thermocouple was used to measure temperature. A total of 10 mg of the catalysts (53−125 μm) diluted with inert 250 mg of α-Al_2O_3 (53−125 μm) was loaded in the catalyst's bed. A series of mass flow controllers (Bronkhorst) allowed us to feed reactant gases of CH_4, CO_2, H_2, and Ar. A gas chromatograph (Agilent, GC6890N) equipped with a TCD detector, using helium as the carrier gas, was applied to analyze different gas species online including CH_4, CO_2, H_2, CO, and Ar. First, the catalysts were reduced at 670 °C for 16 h in a mixture of H_2/Ar (H_2/Ar = 50:50 mL/min). In the activity test and selectivity test, the reaction temperature increased from 450 °C to 800 °C with an interval of 50 °C (CH_4/CO_2/Ar = 30:30:140 mL/min, GHSV = 180,000 $mL_{CH_4}\cdot h^{-1}\cdot g_{cat}^{-1}$), and the output data from the gas chromatograph were collected under the steady state for around 30 min at every temperature. Additionally, stability test was performed at 700 °C for 30 h (CH_4/CO_2/Ar = 60:60:30 mL/min).

All the experiments were performed at the kinetic region, and external and internal diffusion limitation was eliminated under the reaction conditions. The CO_2 and CH_4 conversions (X_{CO_2} and X_{CH_4}), H_2/CO ratio, net reaction rate (r_n), forward reaction rate, (r) and turnover frequency (TOF) were calculated under the differential conditions as follows

$$X_{CO_2} = \frac{F_{CO_2,in} - F_{CO_2,out}}{F_{CO_2,in}} \quad (1)$$

$$X_{CH_4} = \frac{F_{CH_4,in} - F_{CH_4,out}}{F_{CH_4,in}} \quad (2)$$

https://dx.doi.org/10.1021/acscatal.0c04429
ACS Catal. 2021, 11, 2398−2411

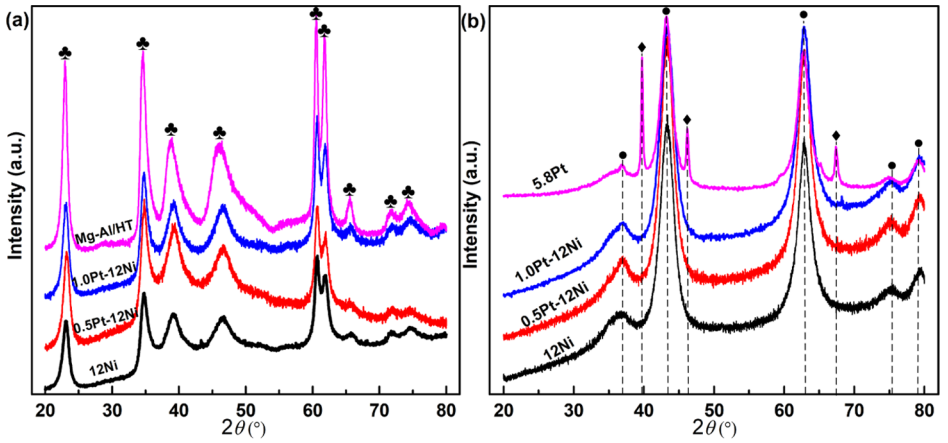

Figure 1. XRD patterns of (a) as-prepared hydrotalcite-like precursors and (b) calcined samples. (Black suit) Hydrotalcite-like structure; (black circle) mixed oxide NiO−Mg(Al)O; (black diamond) Pt species.

$$H_2/CO = \frac{F_{H_2,out}}{F_{CO,out}} \tag{3}$$

$$r = \frac{r_n}{1-\eta} \tag{4}$$

$$TOF = \frac{r \cdot M_i}{f_i, D} = \frac{r \cdot M_{Pt+Ni}}{f_{Pt+Ni} \cdot D}(s^{-1}) \tag{5}$$

where $F_{i,in/out}$ is the volume fraction of each species for the feed gas (in) and the effluent gas (out), W is the weight of the catalyst, η is the approach to equilibrium, M_i is the molecular weight of Ni and Pt in weighted average, and f_i is the total metal (Ni and Pt) weight fraction of catalysts. The dispersion D was estimated based on the total metal (Ni and Pt) surface area of catalysts measured by hydrogen chemisorption.

2.3. Computational Methods. All the DFT calculations were performed with a periodic slab model using Vienna Ab initio Simulation Program (VASP).[39,40] The generalized gradient approximation (GGA) and the BEEF-vdW exchange−correlation functional were used in the calculations.[41] The electron−ion interaction was described by the projector augmented wave (PAW) method.[42] The compact convergence of plane-wave cutoff energy was set as 400 eV. The self-consistent lattice constant of 3.540 Å (3.52 Å[43]) is used for Ni bulk and 3.982 Å (3.92 Å[44]) is used for Pt bulk. Moreover, five atomic layers of the Ni(111) and Pt(111) surface were cleaved at a $p(3 \times 3)$ supercell. The top three layers and the adsorbates were allowed to relax, while the bottom two layers were fixed at their equilibrium bulk positions. 1/9Pt−Ni(111) and 3/9Pt−Ni(111) were modeled based on the optimized Ni(111). Figure S1 (Supporting Information) depicts the four models of catalysts. Because of the magnetic moment of Ni, spin-polarized electrons have been considered for Ni(111) and the Pt−Ni bimetallic surface. A 15 Å vacuum region and a Fermi smearing of 0.2 eV were applied in this work. The meshes of $5 \times 5 \times 1$ k-points were used for the Ni, Pt, and Pt−Ni surfaces using the Monkhorst−Pack method.[45] Furthermore, transition states were searched by the dimer method,[46] and only one imaginary frequency was identified for each transition state.

Adsorption energy (E_{ads}) and activation barrier (E_a) are given by

$$E_{ads} = E_{adsorbate/surface} - E_{adsorbate} - E_{surface} \tag{6}$$

$$E_a = E^{TS} - E^{IS} \tag{7}$$

where $E_{adsorbate/surface}$ is the total energy of the surface with the adsorbate adsorbed, $E_{adsorbate}$ is the total energy of the isolated adsorbate, $E_{surface}$ is the total energy of the bare surface, E^{TS} is the total energy of the transition state, and E^{IS} is the total energy of the initial state.

3. RESULTS AND DISCUSSION

3.1. Texture and Chemical Properties of Bimetallic Catalysts. X-ray diffraction patterns of the prepared hydrotalcite-like precursors and calcined samples are shown in Figure 1a,b, respectively. In Figure 1a, XRD patterns of fresh hydrotalcite-like samples exhibit typical reflections at 2θ = 23.5°, 35°, 60.5°, and 61.9°, corresponding to the (006), (009), (110), and (113) planes in the multilayer hydrotalcite structure.[35] The patterns of the calcined samples (Figure 1b) show three primary reflections at around 2θ = 36°, 43.5°, and 63°, indicating the structure of Ni−Mg−Al mixed oxides,[34,35] respectively. In the case of Pt-added hydrotalcite-derived catalysts, some reflections could be observed at around 38°, 46.5°, and 68°, corresponding to the (111), (200), and (220) planes for Pt phase,[24,25,47] respectively.

Results in Figure 1b indicated that the calcination at the high temperature (600 °C) destroyed the hydrotalcite layer structure and formed the mixed oxide. When it was treated in Pt-containing solution, the mixed oxides transferred back to the layered structure due to the memory effect[35] of the hydrotalcite. Re-calcination transferred the layered structure again to the mixed oxide. The XRD patterns of the reduced and passivated Pt−Ni catalysts are almost identical to those of calcined ones, which are not presented here for a reason of clarity.

As seen in Figure S2a, the N_2 adsorption/desorption isotherms of calcined catalysts are typical of mesoporous materials.[48−50] Obviously, the process re-layering the hydrotalcite structure and recalcination caused a significant reconstructing, and thus, a different pore structure mainly reduced the mesopores (Figure S2). The BET surface area is between 160 and 200 m^2/g_{cat} for all samples. Compared with the 12Ni sample, 0.5Pt−12Ni and 1.0Pt−12Ni need to be re-calcined after redox reaction and 5.8Pt also requires to be re-calcined after impregnation, leading to the decrease in the

https://dx.doi.org/10.1021/acscatal.0c04429
ACS Catal. 2021, 11, 2398−2411

BET surface area, pore volume, and pore size, as presented in Figure S2b and Table S1.

XRF tests for Ni and Pt catalysts and ICP−MS detections for Pt−Ni catalysts indicate that we have synthesized the catalysts with expected metal loadings for both the monometallic and the bimetallic. The dispersions for Pt−Ni bimetallic catalyst samples are all lower than those of the Ni catalyst. In addition, a similar trend is acquired for the metallic surface area; the details are provided in Table 1.

Table 1. Metal Loading, Metallic Surface Area, and Total Dispersion of Calcined Catalysts

catalyst	Ni loading [wt %]	Pt loading [wt %]	metallic surface area [m^2/g_{cat}]	total dispersion [%]	particle size TEM [nm]
12Ni	12.0 (11.0[a])	0	12.21	15.28	8.1
0.5Pt−12Ni	12.0 (13.0[b])	0.5 (0.5[b])	8.46	10.43	0.6
1.0Pt−12Ni	12.0 (13.2[b])	1.0 (0.9[b])	8.80	10.68	0.4
5.8Pt	0	5.8 (4.8[a])	9.72	67.88	1.1

[a]XRF results. [b]ICP−MS results.

The transmission electron microscopy (TEM) images of the 12Ni, 5.8Pt, 0.5Pt−12Ni, and 1.0Pt−12Ni catalysts are presented in Figure 2. As for the neat Ni sample, the average particle size of 12Ni is around 8.0 nm. In addition, fringes of 0.200 nm[S1] of metallic Ni^0 are attributed to (111) planes. The average crystal size of the Pt catalyst is about 1 nm (Figure 2d,e). The atomic resolution imaging of the 0.5Pt−12Ni and 1.0Pt−12Ni bimetallic catalysts is shown in Figure 2g,h and Figure 2j,k, respectively. The bright dots in the TEM images represent Ni and Pt atoms. Unfortunately, it is impossible to clearly distinguish between the Ni and Pt atoms in the image because they are mixed evenly. The average particle sizes of bimetallic Pt−Ni catalysts that are limited to 0.5 nm are much smaller than those of the pure Ni (about 8 nm) and neat Pt sample (about 1.1 nm). There are a lot of single atoms, dimers, and subnanometer-sized clusters observed. The average particle size of the 1.0Pt−12Ni bimetallic cluster (about 0.4 nm) is even smaller than the one of 0.5Pt−12Ni (about 0.6 nm). Such small clusters of Pt−Ni bimetallic catalysts are most likely a result of the recycling of highly acidic Pt precursors in the Ni catalyst bed. The reduced Ni might dissolve in the solution and redisperse on the support. The results reveal that the surface redox reaction with the recycling of the solution is an efficient way to prepare highly dispersed, even atomically dispersed, bimetallic catalysts at high loadings.

It should be noticed that there is a large deviation between the particle size measured by TEM and the dispersion estimated by chemisorption for Pt−Ni bimetallic catalysts. It could be caused by a weak dissociation and adsorption of hydrogen on cation bimetallic catalysts. The small clusters strongly bonded to the support, which could exist as cations.

H_2 temperature-programmed reaction (TPR) profiles of the calcined Ni, Pt−Ni, and Pt catalysts are shown in Figure S3, to compare the reduction behavior of calcined samples. Calcined Ni exhibits one main peak at 850 °C due to the reduction of NiO species into Ni^0, which has been reported

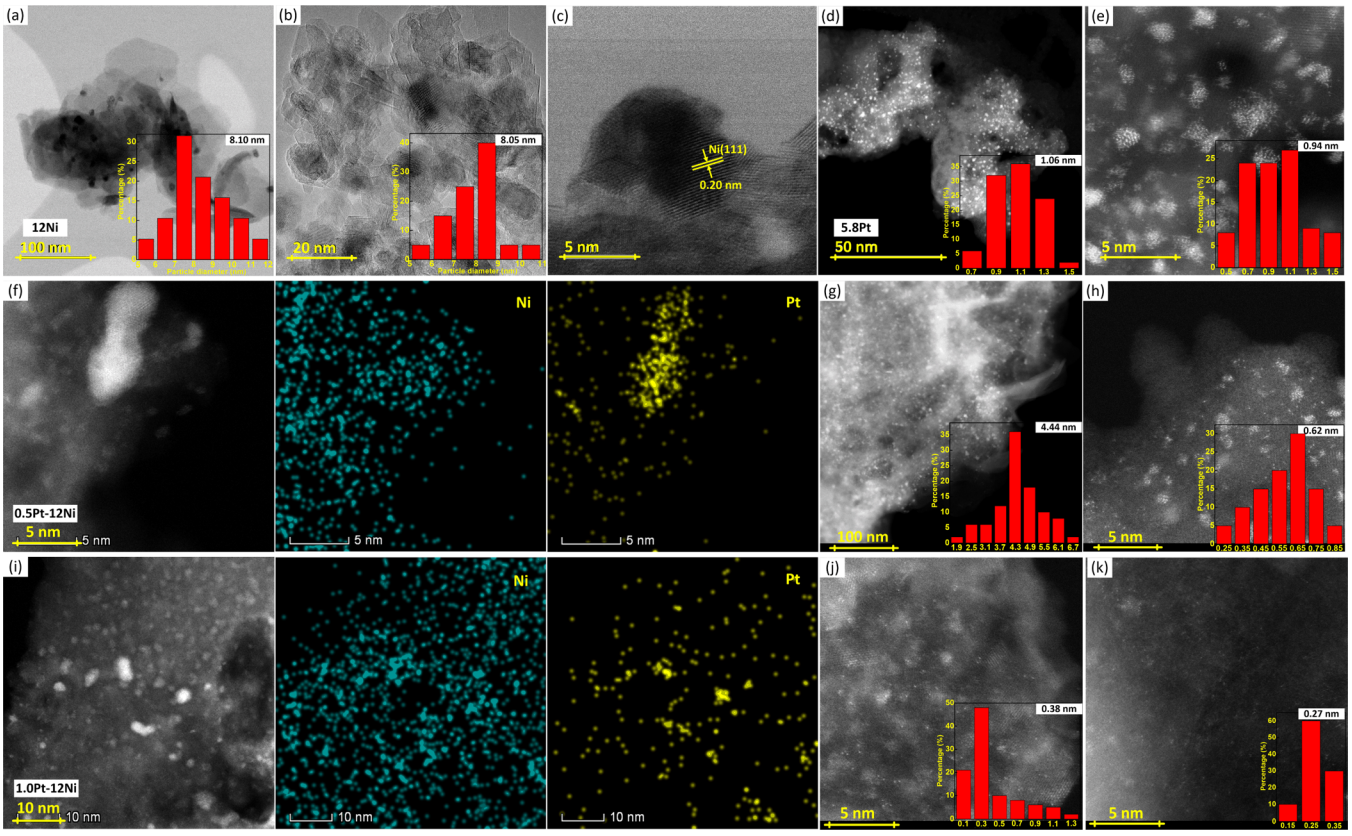

Figure 2. TEM images of (a−c) Ni, (d,e) Pt, (g,h) 0.5Pt−12Ni, and (j,k) 1.0Pt−12Ni. EDX mapping of (f) 0.5Pt−12Ni and (i) 1.0Pt−12Ni.

https://dx.doi.org/10.1021/acscatal.0c04429
ACS Catal. 2021, 11, 2398−2411

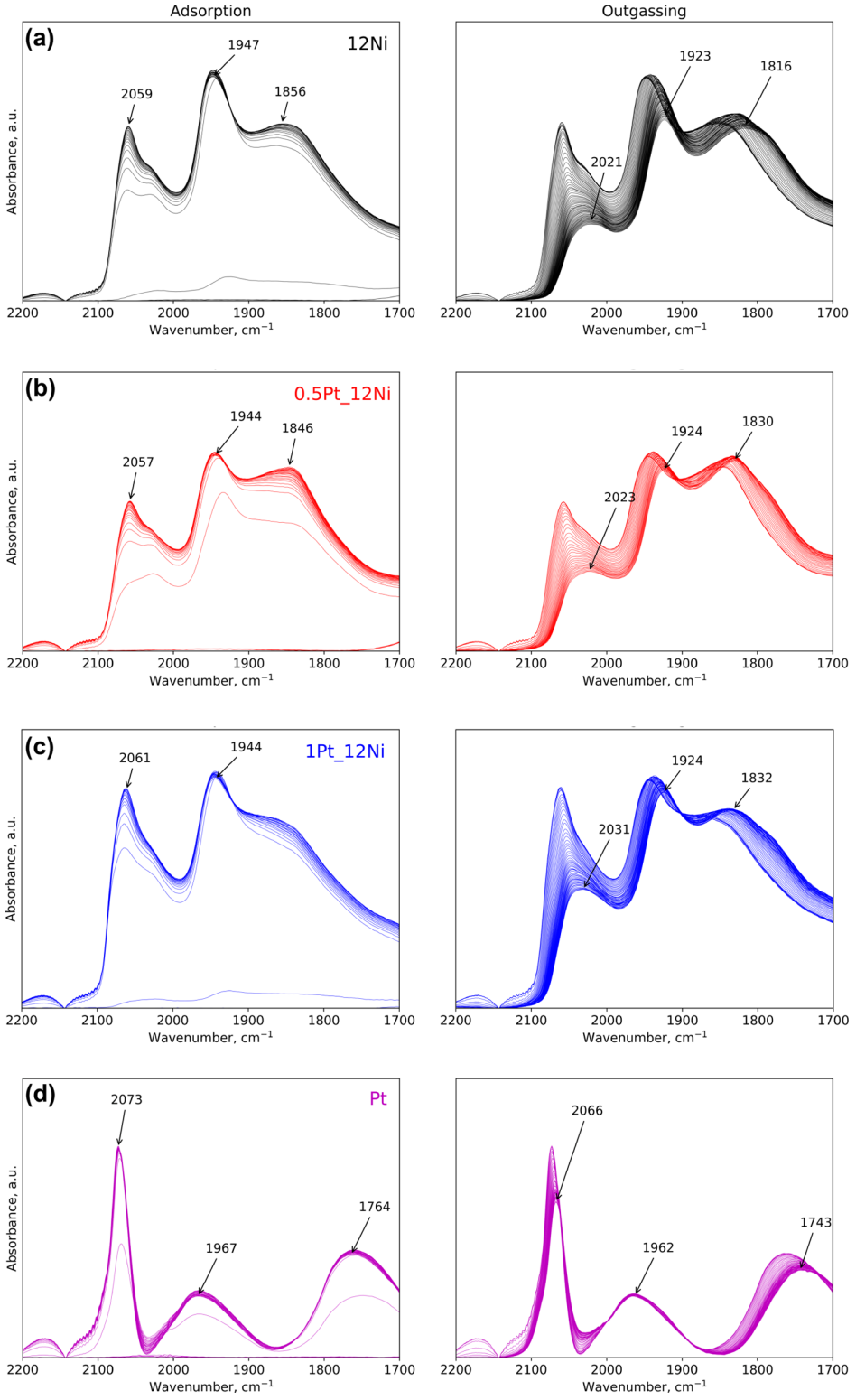

Figure 3. DRIFT spectra of CO adsorption on reduced (a) 12Ni/Mg(Al)O; (b) 0.5Pt−12Ni/Mg(Al)O; (c) 1.0Pt−12Ni/Mg(Al)O; and (d) 5.8Pt/Mg(Al)O at ambient temperature.

in previous studies.[35] Such Ni-oxide species are most likely to insert into the Mg−Al mixed oxide matrix resulting from the calcination of the hydrotalcite brucite layers, forming a solid solution of high thermal stability. It is attributed to a strong interaction between Ni and the Mg−Al oxide matrix.[52,53] Besides, this peak maximum shifted to lower temperatures with an increase in Pt loading. The increasing Pt loading is in favor of the reduction and lowers reduction temperatures of Ni catalysts. It suggests that there exists a synergistic interaction between two metals, which could be attributed to introducing platinum atoms into the surface of nickel particles, causing hydrogen spillover, thus promoting the Ni^{2+} reduction.[54,55] It might indicate the formation of Pt−Ni bimetallic catalysts.

https://dx.doi.org/10.1021/acscatal.0c04429
ACS Catal. 2021, 11, 2398−2411

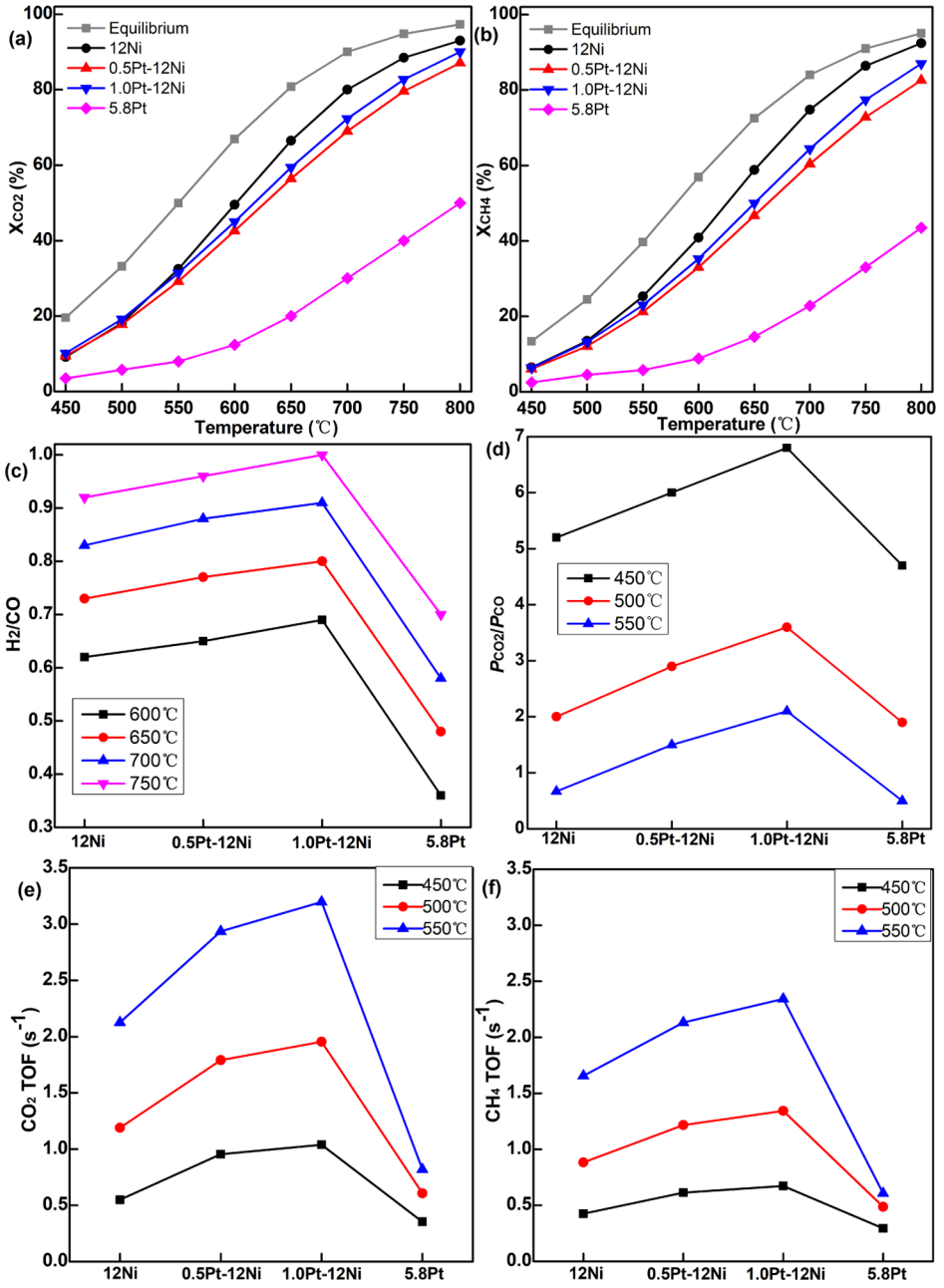

Figure 4. (a) CO_2 conversion X_{CO_2}; (b) CH_4 conversion X_{CH_4}; (c) H_2/CO ratio; (d) P_{CO_2}/P_{CO}; (e) TOF of CO_2; and (f) TOF of CH_4. Reaction conditions: $CO_2/CH_4/Ar$ = 30/30/140 mL/min and $GHSV_{CH_4}$ = 180,000 mL·h^{-1}·g$_{cat}^{-1}$.

Ni 2p spectra for bimetallic Pt−Ni samples are depicted in Figure S4. For 0.5Pt−12Ni, Ni 2p XPS spectra possessed two spin−orbit doublets of Ni at 873.7 (Ni $2p_{1/2}$) and 855.8 eV (Ni $2p_{3/2}$) accompanied with two obvious shakeup satellites, similar to the previous reports on Ni on layered double hydroxides.[56,57] The Ni existed in the oxidized form. The Ni $2p_{3/2}$ is 855.8 eV and 856.4 eV for 0.5Pt−12Ni and 1.0Pt−12Ni, respectively, which are between those of Ni^{2+} (854.7 eV) and Ni^{3+} (856.6 eV).[57−59] The higher oxidation state of Pt−Ni bimetallic clusters than Ni^{2+} might be a result of electron transfer from Pt to Ni in bimetallic clusters.

Diffuse reflectance infrared Fourier transform (DRIFT) spectra based on the CO adsorption at ambient temperature are analyzed and compared for the reduced Ni/Mg(Al)O, Pt/Mg(Al)O, and Pt−Ni/Mg(Al)O catalysts in the range of 2200−1700 cm^{-1}. It has been reported that the peak centered at 2061 cm^{-1} was ascribed to the linear CO adsorption on Ni sites, while that at 1946 and 1873 cm^{-1} was attributed to the CO bonded to bridge Ni sites on Ni/SiO_2.[60−63] Agelli et al., assigned IR peaks more detailed to various adsorbed CO species: 2080−2050 cm^{-1} to sub (di- or tri.) carbonyl ($Ni(CO)_{2,3}$), 2010−2000 cm^{-1} to linear monocarbonyl (Ni−CO), 1950−1800 cm^{-1} to bridge monocarbonyl (Ni_2−CO), and 1875−1800 cm^{-1} to multibonded ($Ni_{3,4}$−CO).[64] As depicted in Figure 3a, the broad band at around 2021 cm^{-1} is assigned to the linear CO species adsorbed on the top site for Ni, while that at 1947 cm^{-1} is assigned to bridge CO adsorption on two Ni atoms. Another peak around 1856 cm^{-1} can be assigned to multibonded CO. With increasing exposure time to CO,

https://dx.doi.org/10.1021/acscatal.0c04429
ACS Catal. 2021, 11, 2398−2411

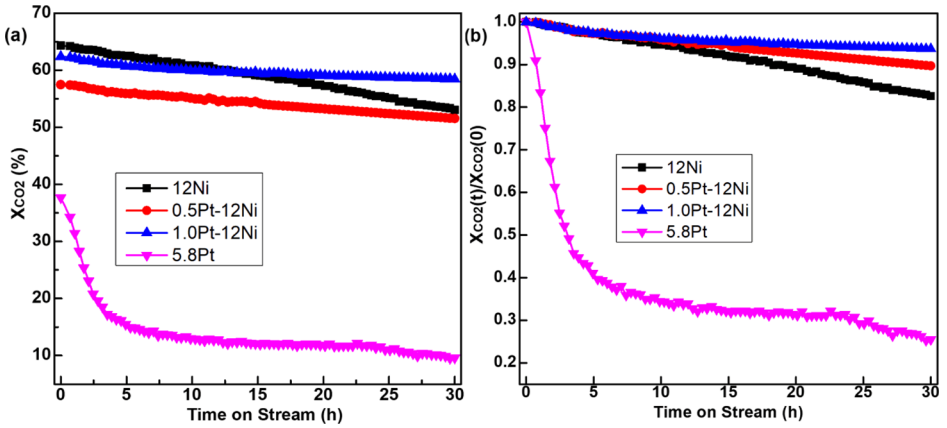

Figure 5. Stability test of catalysts for DRM: (a) CO_2 conversion X_{CO_2} and (b) $X_{CO_2}(T)/X_{CO_2}(0)$. Reaction conditions: CO_2/CH_4/Ar = 60/60/30 mL/min, 700 °C, 1 atm, and 30 h.

the intensity of linear CO adsorption peak increased and the wavenumber shifted to a larger number up to 2059 cm^{-1} due to the formation of sub (di- or tri-)-carbonyl. However, the sub (di- or tri-)-carbonyl is not stable, which disappeared during the degassing process. With the degassing process, the intensity of the multibonded peak increased. For Pt/SiO_2, it has been reported that peaks located in the regions of 2086−2060 cm^{-1} and 1870−1840 cm^{-1} are correlated with the linearly and bridge-adsorbed CO on Pt sites,[65,66] respectively. For Pt/Mg(Al)O (Figure 3d), the peak at 2073−2060 cm^{-1} is assigned to the linear CO species adsorbed on the top site for Pt, while that at 1967 cm^{-1} is assigned to bridge CO adsorption on two Pt atoms. Another peak around 1764 cm^{-1} can possibly be assigned to multibonded CO. Figure 3 reveals the stretching frequency of the strongly adsorbed linear CO and multibonded CO peaks after degassing to higher values with increasing Pt loading, toward the pure Pt catalysts. The IR stretching frequency of the strongly adsorbed linear CO is 2021, 2023, 2031, and 2073 cm^{-1} for 12Ni, 0.5Pt−12Ni, 1.0Pt−12Ni, and 5.8Pt catalysts, respectively. The shifts in the IR stretching frequency of CO are ascribed to partial electron transfer from the metal to the anti-bonding $2\pi^*$ orbital of CO, and the larger shift revels in a large extent of electron transfer with a higher loading of Pt. Besides, for the Pt−Ni catalysts, only one peak on the linear CO adsorption and no separated peaks related to Ni and Pt sites were observed. These results together with the results of TEM, TPR, and XPS suggest the bimetallic Pt−Ni clusters doming for Pt−Ni catalysts. Moreover, the elemental maps obtained by scanning transmission electron microscopy−energy dispersive X-ray spectroscopy (STEM−EDS) further confirm the Pt−Ni catalysts' microscopic composition. There is a strong overlap between the Ni and Pt maps in most of the areas, ensuring Pt−Ni bimetallic cluster formation.

3.2. Activity and Selectivity on the Bimetallic Surface. The kinetic study was performed under the steady-state conditions, heating from 450 to 800 °C with an interval of 50 °C, as seen in Figure 4. The equilibrium conversions of CO_2 and CH_4 are presented in Figure 4, which were calculated through HSC software. Both CH_4−CO_2 reforming and reverse water−gas shift (RWGS) reactions have been considered under the reaction conditions (CO_2/CH_4/Ar = 30/30/140 mL/min, 1 atm), while the solid carbon was not taken into account. In order to acquire the intrinsic conversion (X) of reactants, we use high space velocity to keep it away from thermodynamic equilibrium, as depicted in Figure 4a,b. In general, for all the samples, X_{CO_2} is higher than X_{CH_4} due to the occurrence of side reactions, such as RWGS.[24] The sample 12Ni shows the highest conversions for both reactants. The conversion for the reactant follows the order: 12Ni > 1.0Pt−12Ni > 0.5Pt−12Ni > 5.8Pt. In addition, monometallic Ni and bimetallic Ni-based catalysts have a similar ability for reactant conversion. The differences of conversion between Ni and Pt−Ni catalysts generally show a small increase with the temperature increasing. However, the Pt catalyst has the lowest conversion for the reactant in the whole temperature range.

The selectivity was examined through H_2/CO ratios presented in Figure 4c. Generally, the H_2/CO ratio increases with the temperature increasing. The ratio of conversion for CO_2 to methane decreased toward 1 with increasing temperature. Although the RWGS reaction is an exothermic reaction

$$H_2 + CO_2 \rightarrow CO + H_2O \quad (8)$$

which is thermodynamically favored at high temperatures, the reaction is kinetically suppressed at high temperatures. More interestingly, the H_2/CO ratio depends on the catalysts. Bimetallic Pt−Ni cluster catalysts have a higher H_2/CO ratio than monometallic Ni and Pt samples. Specifically, 1.0Pt−12Ni shows the highest H_2/CO ratio at different temperatures. The H_2/CO ratio is almost 1 at 750 °C, which is the stoichiometric ratio of the neat dry methane reforming, where the conversion of CO_2 and methane is almost identical. Thus, introducing a small amount of Pt into Ni catalysts increases selectivity to hydrogen and suppresses the occurrence of RWGS reaction to reach a higher H_2/CO ratio in the reaction.

To examine the intrinsic effect of Pt in the Pt−Ni bimetallic catalysts, the TOFs were estimated based on the average reaction rate and the surface area of metals measured by chemisorption (Tables S2 and S3). As depicted in Figure 4e,f, both 0.5Pt−12Ni and 1.0Pt−12Ni have higher TOFs compared with monometallic Ni and Pt catalysts. The TOFs increase with increasing Pt content in the bimetals, and 1.0Pt−12Ni shows the highest TOF among the catalysts.

3.3. Coke Resistance on the Bimetallic Surface. Stability tests were performed at 700 °C for 30 h, to compare the deactivation of four samples. Figure 5a displays the X_{CO_2}

https://dx.doi.org/10.1021/acscatal.0c04429
ACS Catal. 2021, 11, 2398−2411

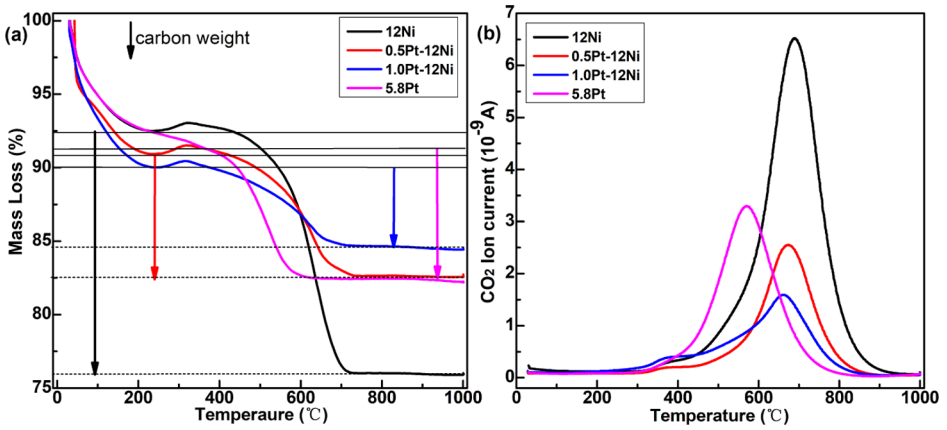

Figure 6. (a) TGA analysis after stability test and (b) CO_2 signal output by MS.

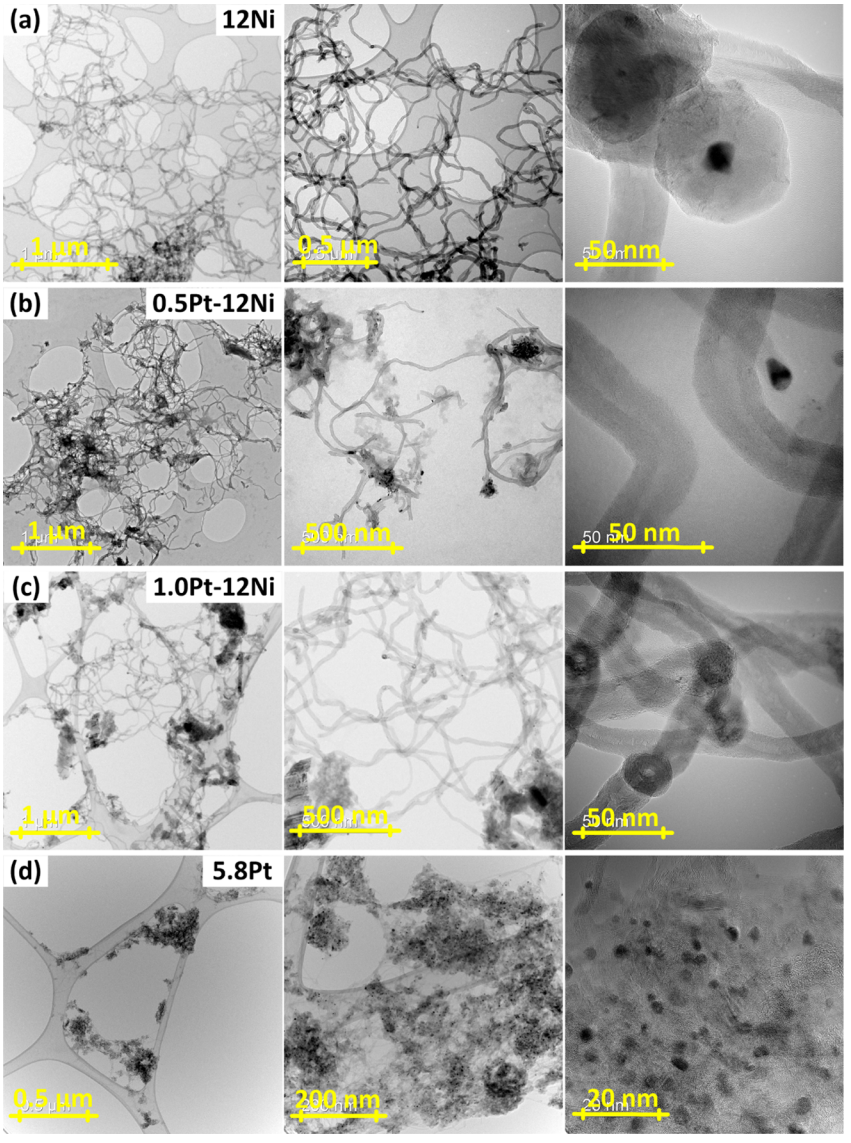

Figure 7. TEM images for different samples after stability test (a) 12Ni; (b) 0.5Pt−12Ni; (c) 1.0Pt−12Ni; and (d) 5.8Pt.

along the 30 h and Figure 5b shows the deactivation function based on $X_{CO_2}(t)/X_{CO_2}(0)$. During the 30 h experimental operation, the initial X_{CO_2} of 12Ni is the highest among the four samples. However, after running for long, X_{CO_2-12Ni} shows a faster decrease compared with the Pt−Ni bimetallic surface; it becomes lower than the $X_{CO_2-1.0Pt-12Ni}$ after 18 h and almost equal to $X_{CO_2-0.5Pt-12Ni}$ after 30 h. We can predict that X_{CO_2-12Ni} would be lower than $X_{CO_2-0.5Pt-12Ni}$, if we keep

https://dx.doi.org/10.1021/acscatal.0c04429
ACS Catal. 2021, 11, 2398−2411

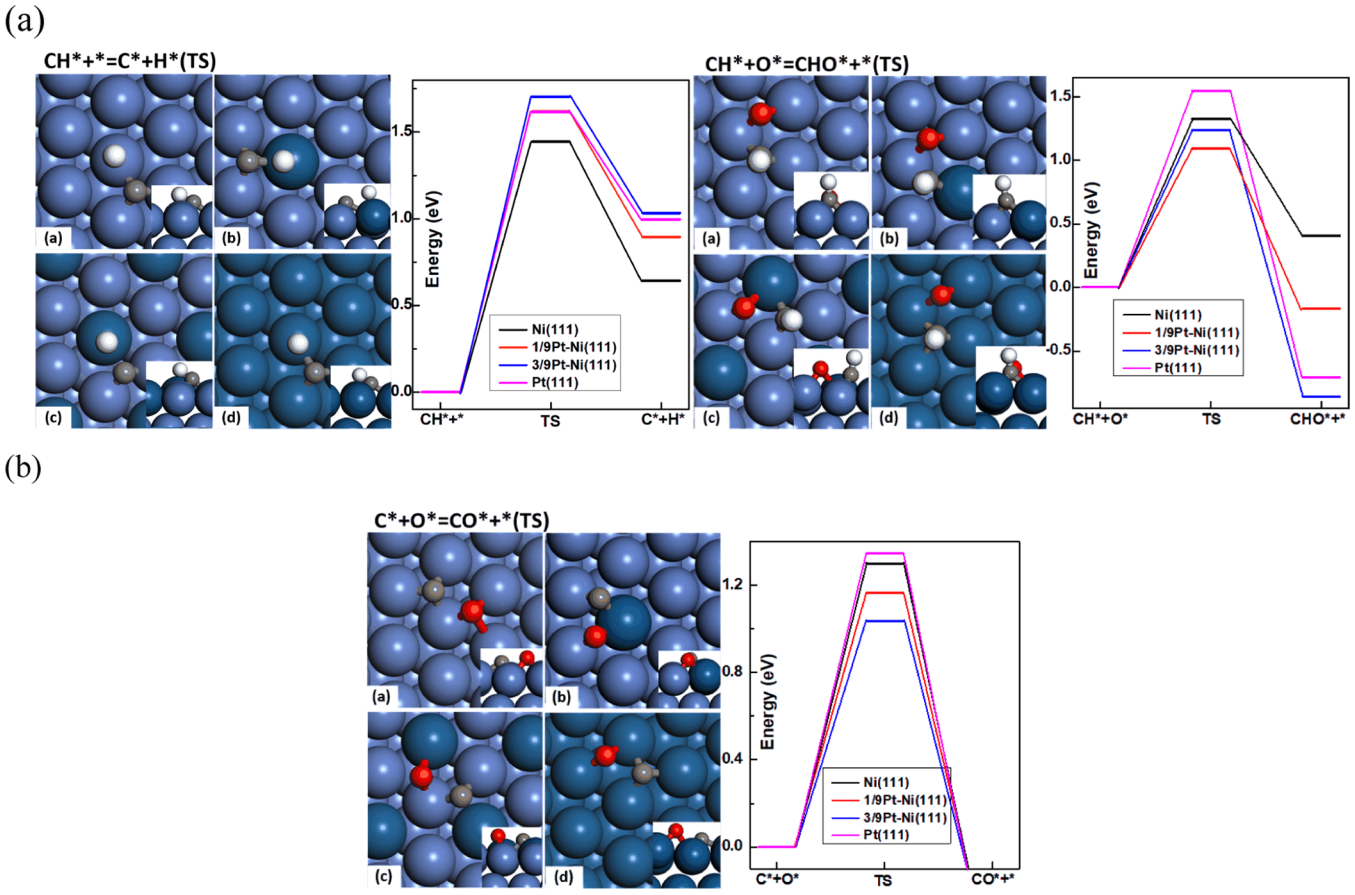

Figure 8. (a) CH dehydrogenation and oxidation and (b) C oxidation on Ni(111), Pt(111), and the bimetallic surface of 1/9Pt−Ni(111) and 3/9Pt−Ni(111).

the experimental running time longer. On the other hand, 5.8Pt deactivated very fast at the beginning due to the Pt sintering at such high temperature. Compared with initial conversion, the final conversions after 30 h running of 12Ni, 0.5Pt−12Ni, and 1.0Pt−12Ni decrease to around 82.5%, 91%, and 94%, respectively. As a consequence, introducing a small amount of Pt onto the Ni surface could significantly improve the ability of the catalyst to resist deactivation, and further investigation and discussion will be provided in the following parts from both experiment analysis and DFT calculation. In addition, the role of Pt in the coke resistance was detected from thermogravimetric analysis−mass spectrometry (TGA−MS) and TEM.

3.3.1. TGA−MS Analysis. The tests were performed under an air stream (50 mL/min), heating from ambient temperature to 1000 °C with a ramping rate of 10 °C/min and dwelling for 30 min at this temperature. The coke amount on the catalysts was measured by the mass loss in TGA curves, proved by MS analysis, as seen in Figure 6. Generally, mass loss curves could be separated into three primary ranges. In the first range (ambient temperature to 220 °C), moisture removal causes the mass loss. In the second range (220−350 °C), a small increase in the weight is attributed to the reduced Ni oxidation. The third range is most important (350−800 °C); the oxidation and removal of coke result in the mass loss, which has been demonstrated by the CO_2 signal output by MS detection. Specifically, the percentage of the carbon amount in four samples after the stability test follows the order 12Ni > 5.8Pt > 0.5Pt−12Ni > 1.0Pt−12Ni, demonstrating that introducing a small quantity of Pt onto the Ni surface can significantly suppress the coke deposition. Additionally, according to the CO_2 signal, the peak position locates at around 580 °C for 5.8Pt samples, while it shifts to 680 °C for Ni and Pt−Ni samples.

3.3.2. TEM Analysis. Figure 7 shows the TEM images for different samples after the stability test. As for pure Ni catalysts, the formation of coke on the surface is dominated by filamentous carbon. The subordinate carbon species is graphite, which could lead to the deactivation of catalysts. For the pure Pt catalyst, the graphite is dominating on the surface and causes fast deactivation. However, in terms of Pt−Ni samples, the total carbon formation shows a significant decrease compared to those of both Ni and Pt, and coke formation mainly comes from filamentous carbon, which has a little effect on the catalytic activity. Thus, the small amount of Pt addition could markedly enhance the anti-carbon formation performance in the reaction, meanwhile, keeping a higher reaction activity.

3.4. Original Role of Pt in Activity, Selectivity, and Coke Resistance of Pt−Ni. The origin of the role of Pt in Pt−Ni bimetallic catalysts in dry reforming is explored by examining the relationship between the performance of the properties of the catalyst through experimental and DFT study.

3.4.1. DFT Analysis. To investigate the interaction of Pt and Ni in bimetallic catalysts for enhanced activity, selectivity, and stability, DFT studies of the adsorption of key intermediates in the reaction and key elementary steps were

https://dx.doi.org/10.1021/acscatal.0c04429
ACS Catal. 2021, 11, 2398−2411

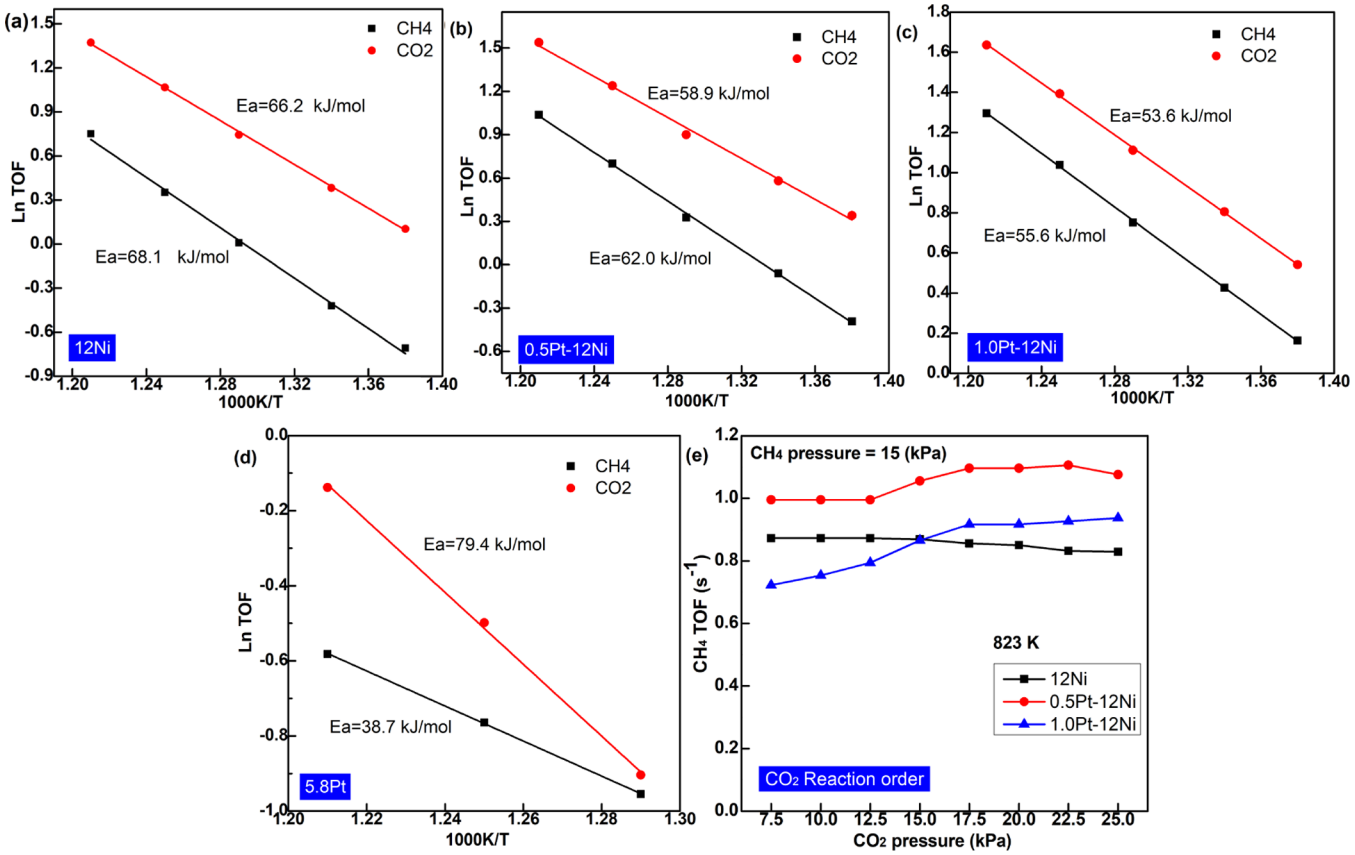

Figure 9. Arrhenius plot (a) 12Ni; (b) 0.5Pt−12Ni; (c) 1.0Pt−12Ni; and (d) 5.8Pt (reaction conditions: $CO_2/CH_4/Ar$ = 30/30/140 mL/min, $GHSV_{CH_4}$ = 360,000 $mL{\cdot}h^{-1}{\cdot}g_{cat}^{-1}$) and (e) changes in methane TOF as a function of CO_2 pressure (823 K, methane pressure of 15 kPa, balance Ar, total pressure = 100 kPa).

performed on Ni, Pt, 1/9Pt−Ni, and 3/9Pt−Ni models. The slab model was used to describe the structure of bimetallic catalysts. Although this model may not be fully representative of the actual structure of Pt−Ni, DFT calculations provide a suitable understanding of the reaction mechanism. The adsorption heat of the key intermediates in the reaction such as CH*, C*, CO*, H*, O*, and OH* is presented in Figure S5. The binding energies of C*, CH*, and CO* in the bimetallic Pt−Ni catalysts are lower than those in Ni and Pt, and the binding energy decreased with increasing Pt fraction in bimetallic catalysts. The electronic structure of Ni is modified by charge transfer from Ni to Pt, which decreases the electron density of the Pt d-orbital, weakening the interaction between the Pt−Ni surface and adsorbed carbon-containing intermediates. The O* adsorption heat behaves differently from the C* adsorption heat and follows an order of Ni > 1/9Pt−Ni > 3/9Pt−Ni > Pt. It should be noted that the composition of the bimetallic catalyst in DFT calculation does not reflect the exact one, but it presents well the tendency of the effect of Pt.

3.4.2. Role of Pt in Coke Resistance. It has been pointed out that the formation of carbon, including the filamentous carbon and the encapsulating carbon, depends on the surface carbon concentration, where surface carbon C* is the precursor for carbon formation.[67] A decrease in the surface C* formation can in principle reduce the carbon formation. The Pt−Ni bimetallic surface shows the lower binding energy of C* and O* (Figure S5), which can change the surface elementary reactions involved in the formation and consumption of C*. We have previously also shown that CH* is the common intermediate leading competitively to C* and CO* formation. There are two types of competitive reactions: (1) competition in CH* conversion between C* (CH* + * = C* + H*) and CHO* (CH* + O* = CHO* + *) formation and CHO* being the intermediate leading to CO formation; (2) competition between the C* formation and gasification (C* + O* = CO* + *) by the reactions of CH* decomposition or hydrogenation and CH* + O* reaction, respectively. The effects of bimetallic Pt−Ni on the three elementary reaction steps were then analyzed by DFT. As seen in Figure 8a, the energy barrier for CH* decomposition leading to surface carbon C* formation on 3/9Pt−Ni(111) remarkably increases to 1.705 eV compared with Ni(111). Meanwhile, the energy barriers for both CH and C oxidation are lowest on 3/9Pt−Ni(111), while the energy barrier for CH* + O* reaction is lower on Pt−Ni surfaces than on the Ni(111). In addition, the energy barrier for gasification of the surface carbon (C* + O*) is also lower on Pt−Ni surfaces compared to that on Ni(111), as provided in Figure 8b. The lower energy barrier for CH* + O* and C* + O* means a higher reactivity. Besides the O* reactivity, the O* surface concentration is another important factor for the reaction rates. The CO_2 decomposition (CO_2* + * = CO* + O*) is often close to equilibrium; then, the surface O* potential or the surface oxygen density has a positive linear correlation with the ratio of P_{CO_2}/P_{CO} described by eq 7.[68]

https://dx.doi.org/10.1021/acscatal.0c04429
ACS Catal. 2021, 11, 2398−2411

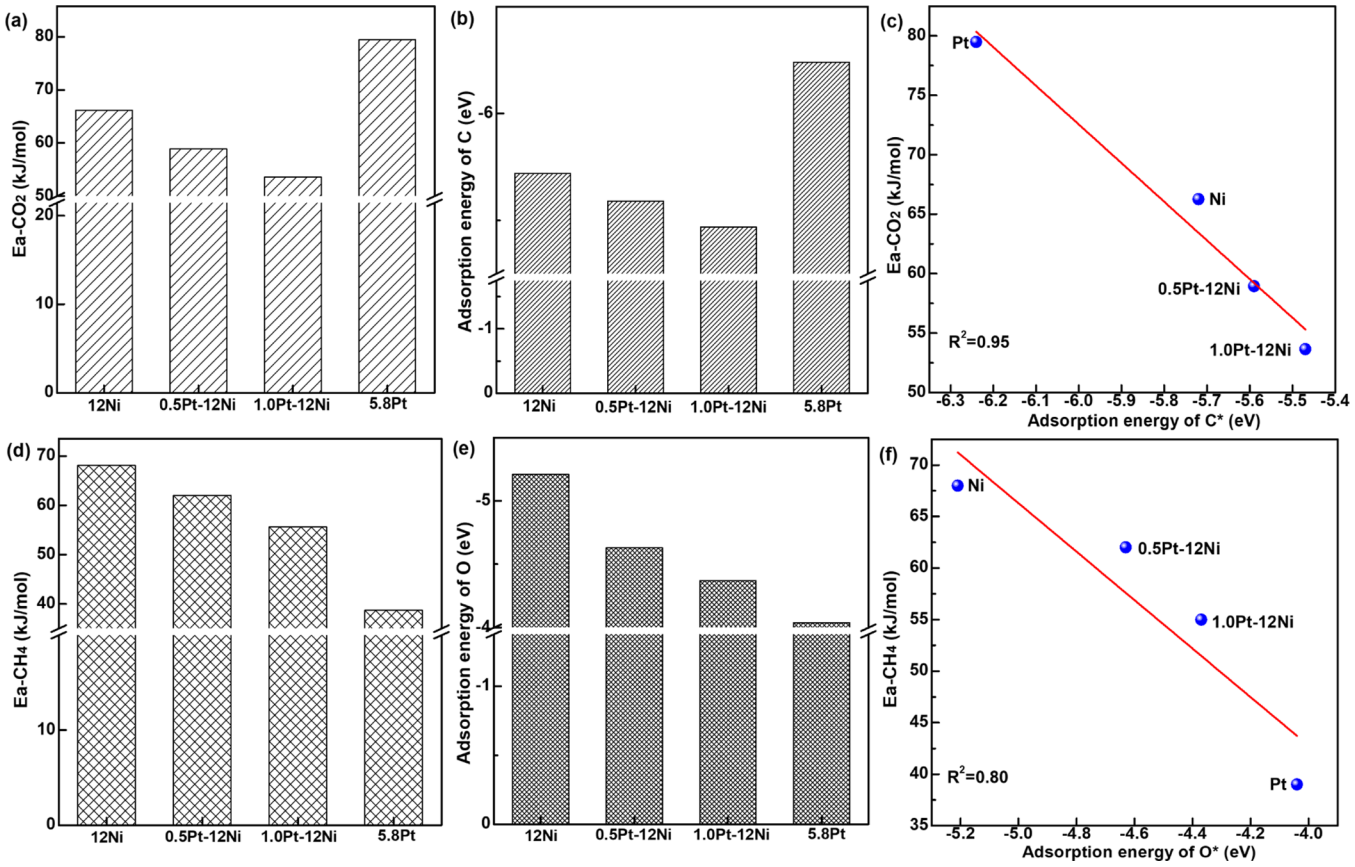

Figure 10. Plot of (a) activation energy of CO_2; (b) adsorption heat of C; (c) linear relationship between activation energy of CO_2 and adsorption heat of C; (d) activation energy of CH_4; (e) adsorption heat of O, and (f) linear relationship between activation energy of CH_4 and adsorption heat of O as a function of catalysts.

$$[O]/* = P_{CO_2}/P_{CO}/K \quad (9)$$

As seen in Figure 4d, P_{CO_2}/P_{CO} ratios on bimetallic samples are all higher than those on neat Ni and Pt catalysts, and P_{CO_2}/P_{CO} on 1.0Pt−12Ni is the highest among the four samples at different reaction temperatures. It indicated that the addition of Pt on the Ni particle surface could enhance the surface oxygen (O*) density. The higher O* concentration and O* reactivity and the higher barrier for CH* decomposition to C* + H* on Pt−Ni surfaces result in a lower rate of surface carbon formation compared to Ni and Pt surfaces. Therefore, the DFT analysis rationalizes well the experimentally observed synergy of bimetallic Pt−Ni in coke resistance of dry reforming, where the rate of carbon formation is lower on Pt−Ni catalysts than on neat Ni and Pt catalysts, and the higher Pt fraction in Pt−Ni bimetallic catalysts results in a lower carbon formation rate.

For the neat Pt catalyst, the energy barrier of CH decomposition is similar to that for the Pt−Ni surface and higher than for Ni(111), while the C*+O* barrier on Pt(111) is the highest among the four surfaces. It explains that the rate of carbon formation is lower than in Ni but higher than in the Pt−Ni catalyst.

3.4.3. Role of Pt in Selectivity. The nature of the suppression of RWGS on Pt−Ni catalysts was examined by DFT calculation. The adsorption energy of the most important adsorbates is presented in Figure S5. The binding energy of H* on the Pt−Ni bimetallic surface is lower than that of monometallic Ni and Pt catalysts. In addition, as depicted in Figure S6, the lower binding energy of H* on the 3/9Pt−Ni(111) favored the combination of H* for H_2 formation and disfavored the hydrogen dissociation compared to that of Ni(111). As a consequence, it enhanced hydrogen formation and reduced RWGS.

3.4.4. Role of Pt in Activity. In order to gain an in-depth insight into the effect of the Pt−Ni bimetal on the catalytic performance, kinetic experiments were performed at the methane flow-based GHSV of 360,000 $mL_{CH_4}\cdot h^{-1}\cdot g_{cat}^{-1}$ from 723 to 823 K with an interval of 25 K. Apparent activation energy and the CO_2 reaction order for Ni and Pt−Ni catalysts have been measured by the Arrhenius plot in Figure 9. The estimated apparent activation energy on pure Ni catalysts for CH_4 and CO_2 is 68.1 kJ/mol and 66.2 kJ/mol, respectively, which is in good agreement with the previously reported value of 70.6 kJ/mol and 64.8 kJ/mol, respectively.[69] The activation energy of CO_2 decreases from 66.2 kJ/mol on the neat Ni to 58.9 kJ/mol and 53.6 kJ/mol on 0.5Pt−12Ni and 1.0Pt−12Ni, respectively. As for CH_4 activation, the activation energy is 55.6 kJ/mol on 1.0Pt−12Ni, much lower than that of 68.1 kJ/mol on Ni.

Figure 9e depicts the effect of CO_2 partial pressure on CH_4 forward reaction rate. For the neat Ni catalysts, the CH_4 forward reaction rate is constant, regardless of CO_2 pressure. It suggests the CO_2 reaction order approaching 0, which agrees with the previous report where methane dissociation is the rate-determining step.[70] However, the complex CO_2 pressure dependence of the methane forward reaction rate is seen in Pt−Ni catalysts. In general, a slight increase in the

https://dx.doi.org/10.1021/acscatal.0c04429
ACS Catal. 2021, 11, 2398−2411

methane forward reaction rate was observed with increasing CO_2 pressure. It reveals that the surface oxidation step leading to CO formation (possibly CH* + O*) became the kinetically relevant step on Pt−Ni bimetallic catalysts.

Significant activation energy dependence of the catalyst composition can be ascribed to the electronic modification by forming the Pt−Ni bimetallic surface. The tendency in changes in the methane activation energy lies well with the tendency of the shift of CO stretching frequency due to the charge transfer between Pt and Ni (Figure 2), as discussed above. Besides, the tendency of the CO_2 activation energy is similar to the tendency of C* adsorption energy with catalyst composition calculated by DFT (Figure 10a,b), while the tendency of the methane activation energy is similar to the tendency of O* adsorption energy (Figure 10d,e). It points out that there is a relationship between the apparent activation energy and the adsorption heat of C* or O*. Activation energy of CO_2 increases with the C* adsorption energy increasing (Figure 10c), and activation energy of CH_4 increases with the O* adsorption energy increasing (Figure 10f). Bimetallic Pt−Ni caused a reduction in the oxygen-binding energy and introduced a contribution of surface oxidation into the kinetically relevant steps and a reduction in the apparent activation energy.

Results reveal that the small amount of Pt addition could markedly lower the energy for CO_2 activation. It will promote the CO_2 dissociation into CO* and O* on the surface of catalysts. In addition, the occurrence of O* plays the key role in the oxidation of CH_x and surface carbon, which will affect the H_2/CO ratio of the product and the amount of the coke formation. Bimetallic (1.0Pt−12Ni) clusters reduce the activation energy for CH_4 dissociation and enhance the catalytic activity and lower the energy barrier for CO_2 activation and promote the formation of surface O* by CO_2 adsorptive dissociation, which has been demonstrated in Figure 4d. The bimetallic Pt−Ni could enhance surface oxygen density. It is beneficial to improve the resistance to coke formation of the catalyst and prolong its service life in the reaction process.

4. CONCLUSIONS

The Pt−Ni bimetallic catalysts enhanced activity, selectivity, and coke resistance in dry reformation compared to neat Ni and Pt ones. The formation of Pt−Ni bimetallic clusters was examined by TEM, SEM, XPS, TPR, and FTIR-CO adsorption and desorption. We unraveled the original role of Pt in the enhanced catalytic performance of the bimetallic clusters by combining DFT and kinetic study. We identified modification of the electronic structure playing a vital role in the bimetallic catalyst, which weakened the adsorption of adsorbed species. The bimetallic Pt−Ni yielded the lower adsorption energy of H* and carbon-containing species such as CO*, C*, and CH*, compared to Ni(111) and Pt(111). The catalytic consequence of such a modification of the bimetallic catalyst can be ascribed as that one stone killed three birds. In detail, the bimetallic catalyst reduced the activation energy of methane and CO_2, leading to a higher activity, enhanced surface O* reactivity, and oxygen surface concentration, leading to a higher coke resistance, and weakened the hydrogen dissociation and enhanced the hydrogen formation, thus leading to a suppressed RWGS and a higher H_2/CO. The enhanced O* reactivity contributed to the high activity and surface C* cleaning and thus a high coke resistance.

This work provides new insights into Pt−Ni bimetal catalysts in improving the activity, selectivity, and stability in DRM from both experimental observations and DFT calculations and are helpful to give some guidance for the synthesis of novel bimetallic Ni-based catalysts for better DRM performance.

■ ASSOCIATED CONTENT

Supporting Information

The Supporting Information is available free of charge at https://pubs.acs.org/doi/10.1021/acscatal.0c04429.

Detailed information of the instrument type and reaction conditions for Ni, Pt, and Pt−Ni catalyst characterizations, detailed characterizations (N_2 adsorption, H_2-TPR, and XPS) for the various catalyst structures, experimental tests (CO_2 and CH_4 average reaction rate), and DFT calculations (catalyst's model, adsorption energy, and energy profiles for H_2 formation and dissociation) (PDF)

■ AUTHOR INFORMATION

Corresponding Author

De Chen − *Department of Chemical Engineering, Norwegian University of Science and Technology, Trondheim 7491, Norway;* orcid.org/0000-0002-5609-5825; Email: de.chen@ntnu.no

Authors

Juntian Niu − *Key Laboratory of Low-grade Energy Utilization Technologies and Systems, Ministry of Education of PRC, Chongqing University, Chongqing 400044, China; Department of Chemical Engineering, Norwegian University of Science and Technology, Trondheim 7491, Norway*

Yalan Wang − *Department of Chemical Engineering, Norwegian University of Science and Technology, Trondheim 7491, Norway*

Shirley E. Liland − *Department of Chemical Engineering, Norwegian University of Science and Technology, Trondheim 7491, Norway*

Samuel K. Regli − *Department of Chemical Engineering, Norwegian University of Science and Technology, Trondheim 7491, Norway*

Jia Yang − *Department of Chemical Engineering, Norwegian University of Science and Technology, Trondheim 7491, Norway*

Kumar R. Rout − *SINTEF Materials and Chemistry, Trondheim 7491, Norway*

Jun Luo − *Center for Electron Microscopy and Tianjin Key Lab of Advanced Functional Porous Materials, Institute for New Energy Materials, School of Materials, Tianjin University of Technology, Tianjin 300384, China;* orcid.org/0000-0001-5084-2087

Magnus Rønning − *Department of Chemical Engineering, Norwegian University of Science and Technology, Trondheim 7491, Norway;* orcid.org/0000-0002-6116-6659

Jingyu Ran − *Key Laboratory of Low-grade Energy Utilization Technologies and Systems, Ministry of Education of PRC, Chongqing University, Chongqing 400044, China*

Complete contact information is available at:

https://dx.doi.org/10.1021/acscatal.0c04429
ACS Catal. 2021, 11, 2398−2411

https://pubs.acs.org/10.1021/acscatal.0c04429

Notes

The authors declare no competing financial interest.

■ ACKNOWLEDGMENTS

The authors would like to thank the project supported by the China Postdoctoral Science Foundation (no. 2020M683241), Natural Science Foundation of Chongqing (no. cstc2020jcyj-msxmX0454), Fundamental Research Funds for the Central Universities (no. 2020CDJ-LHZZ-049), Chongqing Special Postdoctoral Science Foundation (no. XmT2019008), National Natural Science Foundation of China (no. 51976019), China Scholarship Council (no. 201606050054), and Department of Chemical Engineering in Norwegian University of Science and Technology, Norway, and the Notur project supporting the computational time.

■ REFERENCES

(1) Song, Y.; Ozdemir, E.; Ramesh, S.; Adishev, A.; Subramanian, S.; Harale, A.; Albuali, M.; Fadhel, B. A.; Jamal, A.; Moon, D.; Choi, S. H.; Yavuz, C. T. Dry reforming of methane by stable Ni−Mo nanocatalysts on single-crystalline MgO. *Science* **2020**, *367*, 777−781.

(2) Peng, H.; Zhang, X.; Han, X.; You, X.; Lin, S.; Chen, H.; Liu, W.; Wang, X.; Zhang, N.; Wang, Z.; Wu, P.; Zhu, H.; Dai, S. Catalysts in coronas: A surface spatial confinement strategy for high-performance catalysts in methane dry reforming. *ACS Catal.* **2019**, *9*, 9072−9080.

(3) Zuo, Z.; Liu, S.; Wang, Z.; Liu, C.; Huang, W.; Huang, J.; Liu, P. Dry reforming of methane on single-site Ni/MgO catalysts: Importance of site confinement. *ACS Catal.* **2018**, *8*, 9821−9835.

(4) Niu, J.; Liland, S. E.; Yang, J.; Rout, K. R.; Ran, J.; Chen, D. Effect of oxide additives on the hydrotalcite derived Ni catalysts for CO_2 reforming of methane. *Chem. Eng. J.* **2019**, *377*, 119763.

(5) Buelens, L. C.; Galvita, V. V.; Poelman, H.; Detavernier, C.; Marin, G. B. Super-dry reforming of methane intensifies CO_2 utilization via Le Chatelier's principle. *Science* **2016**, *354*, 449−452.

(6) Zhao, Y.; Li, H.; Li, H. NiCo@SiO_2 core-shell catalyst with high activity and long lifetime for CO_2 conversion through DRM reaction. *Nano Energy* **2018**, *45*, 101−108.

(7) Niu, J.; Ran, J.; Chen, D. Understanding the mechanism of CO_2 reforming of methane to syngas on Ni@Pt surface compared with Ni(111) and Pt(111). *Appl. Surf. Sci.* **2020**, *513*, 145840.

(8) Niu, J.; Du, X.; Ran, J.; Wang, R. Dry (CO_2) reforming of methane over Pt catalysts studied by DFT and kinetic modeling. *Appl. Surf. Sci.* **2016**, *376*, 79−90.

(9) Kawi, S.; Kathiraser, Y.; Ni, J.; Oemar, U.; Li, Z.; Saw, E. T. Progress in synthesis of highly active and stable nickel-based catalysts for carbon dioxide reforming of methane. *ChemSusChem* **2015**, *8*, 3556−3575.

(10) Fan, C.; Zhu, Y.-A.; Yang, M.-L.; Sui, Z.-J.; Zhou, X.-G.; Chen, D. Density functional theory-assisted microkinetic analysis of methane dry reforming on Ni catalyst. *Ind. Eng. Chem. Res.* **2015**, *54*, 5901−5913.

(11) Pakhare, D.; Spivey, J. A review of dry (CO_2) reforming of methane over noble metal catalysts. *Chem. Soc. Rev.* **2014**, *43*, 7813−7837.

(12) Wang, Z.; Cao, X.-M.; Zhu, J.; Hu, P. Activity and coke formation of nickel and nickel carbide in dry reforming: A deactivation scheme from density functional theory. *J. Catal.* **2014**, *311*, 469−480.

(13) Shang, Z.; Li, S.; Li, L.; Liu, G.; Liang, X. Highly active and stable alumina supported nickel nanoparticle catalysts for dry reforming of methane. *Appl. Catal., B* **2017**, *201*, 302−309.

(14) Črnivec, I. G. O.; Djinovic, P.; Erjavec, B.; Pintar, A. Effect of synthesis parameters on morphology and activity of bimetallic catalysts in CO_2−CH_4 reforming. *Chem. Eng. J.* **2012**, *207*−*208*, 299−307.

(15) Foppa, L.; Margossian, T.; Kim, S. M.; Müller, C.; Copéret, C.; Larmier, K.; Comas-Vives, A. Contrasting the role of Ni/Al_2O_3 Interfaces in water−gas shift and dry reforming of methane. *J. Am. Chem. Soc.* **2017**, *139*, 17128−17139.

(16) De, S.; Zhang, J.; Luque, R.; Yan, N. Ni-based bimetallic heterogeneous catalysts for energy and environmental applications. *Energy Environ. Sci.* **2016**, *9*, 3314−3347.

(17) Li, S.; Gong, J. Strategies for improving the performance and stability of Ni-based catalysts for reforming reactions. *Chem. Soc. Rev.* **2014**, *43*, 7245−7256.

(18) Kim, S. M.; Abdala, P. M.; Margossian, T.; Hosseini, D.; Foppa, L.; Armutlulu, A.; van Beek, W.; Comas-Vives, A.; Copéret, C.; Müller, C. Cooperativity and dynamics increase the performance of NiFe dry reforming catalysts. *J. Am. Chem. Soc.* **2017**, *139*, 1937−1949.

(19) Niu, J.; Wang, Y.; Qi, Y.; Dam, A. H.; Wang, H.; Zhu, Y.-A.; Holmen, A.; Ran, J.; Chen, D. New mechanism insights into methane steam reforming on Pt/Ni from DFT and experimental kinetic study. *Fuel* **2020**, *266*, 117143.

(20) Niu, J.; Ran, J.; Ou, Z.; Du, X.; Wang, R.; Qi, W.; Zhang, P. CO_2 dissociation over Pt_xNi_{4-x} bimetallic clusters with and without hydrogen sources: A density functional theory study. *J. CO_2 Util.* **2016**, *16*, 431−441.

(21) Niu, J.; Ran, J.; Du, X.; Qi, W.; Zhang, P.; Yang, L. Effect of Pt addition on resistance to carbon formation of Ni catalysts in methane dehydrogenation over Pt-Ni bimetallic surfaces: A density functional theory study. *Mol. Catal.* **2017**, *434*, 206−218.

(22) Fan, C.; Zhu, Y.-A.; Xu, Y.; Zhou, Y.; Zhou, X.-G.; Chen, D. Origin of synergistic effect over Ni-based bimetallic surfaces: A density functional theory study. *J. Chem. Phys.* **2012**, *137*, 014703.

(23) Yu, W.; Porosoff, M. D.; Chen, J. G. Review of Pt-based bimetallic catalysis: From model surfaces to supported catalysts. *Chem. Rev.* **2012**, *112*, 5780−5817.

(24) García-Diéguez, M.; Pieta, I. S.; Herrera, M. C.; Larrubia, M. A.; Alemany, L. J. Nanostructured Pt- and Ni-based catalysts for CO_2-reforming of methane. *J. Catal.* **2010**, *270*, 136−145.

(25) García-Diéguez, M.; Finocchio, E.; Larrubia, M. Á.; Alemany, L. J.; Busca, G. Characterization of alumina-supported Pt, Ni and PtNi alloy catalysts for the dry reforming of methane. *J. Catal.* **2010**, *274*, 11−20.

(26) García-Diéguez, M.; Pieta, I. S.; Herrera, M. C.; Larrubia, M. A.; Alemany, L. J. Improved Pt-Ni nanocatalysts for dry reforming of methane. *Appl. Catal., A* **2010**, *377*, 191−199.

(27) Mahoney, E. G.; Pusel, J. M.; Stagg-Williams, S. M.; Faraji, S. The effects of Pt addition to supported Ni catalysts on dry (CO_2) reforming of methane to syngas. *J. CO_2 Util.* **2014**, *6*, 40−44.

(28) Li, L.; Zhou, L.; Ould-Chikh, S.; Anjum, D. H.; Kanoun, M. B.; Scaranto, J.; Hedhili, M. N.; Khalid, S.; Laveille, P. V.; D'Souza, L.; Clo, A.; Basset, J.-M. Controlled surface segregation leads to efficient coke resistant nickel/platinum bimetallic catalysts for the dry reforming of methane. *ChemCatChem* **2015**, *7*, 819−829.

(29) de Miguel, S. R.; Vilella, I. M. J.; Maina, S. P.; San José-Alonso, D.; Román-Martínez, M. C.; Illán-Gómez, M. J. Influence of Pt addition to Ni catalysts on the catalytic performance for long term dry reforming of methane. *Appl. Catal., A* **2012**, *435*−*436*, 10−18.

(30) Dai, C.; Zhang, S.; Zhang, A.; Song, C.; Shi, C.; Guo, X. Hollow zeolite encapsulated Ni−Pt bimetals for sintering and coking resistant dry reforming of methane. *J. Mater. Chem. A* **2015**, *3*, 16461−16468.

(31) Niu, J.; Ran, J.; Qi, W.; Ou, Z.; He, W. Identification of active sites in CO_2 activation on MgO supported Ni cluster. *Int. J. Hydrogen Energy* **2020**, *45*, 11108−11115.

(32) Zhao, Z.-J.; Chiu, C.; Gong, J. Molecular understandings on the activation of light hydrocarbons over heterogeneous catalysts. *Chem. Sci.* **2015**, *6*, 4403−4425.

(33) Marcinkowski, M. D.; Darby, M. T.; Liu, J.; Wimble, J. M.; Lucci, F. R.; Lee, S.; Michaelides, A.; Flytzani-Stephanopoulos, M.; Stamatakis, M.; Sykes, E. C. H. Pt/Cu single-atom alloys as coke-resistant catalysts for efficient C−H activation. *Nat. Chem.* **2018**, *10*, 325−332.
(34) Dębek, R.; Motak, M.; Duraczyska, D.; Launay, F.; Galvez, M. E.; Grzybek, T.; Costa, P. D. Methane dry reforming over hydrotalcite-derived Ni−Mg−Al mixed oxides: the influence of Ni content on catalytic activity, selectivity and stability. *Catal. Sci. Technol.* **2016**, *6*, 6705−6715.
(35) Wang, H.; Blaylock, D. W.; Dam, A. H.; Liland, S. E.; Rout, K. R.; Zhu, Y.-A.; Green, W. H.; Holmen, A.; Chen, D. Steam methane reforming on a Ni-based bimetallic catalyst: density functional theory and experimental studies of the catalytic consequence of surface alloying of Ni with Ag. *Catal. Sci. Technol.* **2017**, *7*, 1713−1725.
(36) He, L.; Berntsen, H.; Chen, D. Approaching sustainable H_2 production: Sorption enhanced steam reforming of ethanol. *J. Phys. Chem. A* **2010**, *114*, 3834−3844.
(37) Fermoso, J.; Rubiera, F.; Chen, D. Sorption enhanced catalytic steam gasification process: a direct route from lignocellulosic biomass to high purity hydrogen. *Energy Environ. Sci.* **2012**, *5*, 6358−6367.
(38) Noor, T.; Gil, M. V.; Chen, D. Production of fuel-cell grade hydrogen by sorption enhanced water gas shift reaction using Pd/Ni-Co catalysts. *Appl. Catal., B* **2014**, *150−151*, 585−595.
(39) Payne, M. C.; Teter, M. P.; Allan, D. C.; Arias, T. A.; Joannopoulos, J. D. Iterative minimization techniques for ab initio total-energy calculations: molecular dynamics and conjugate gradients. *Rev. Mod. Phys.* **1992**, *64*, 1045−1097.
(40) Delley, B. Fast calculation of electrostatics in crystals and large molecules. *J. Phys. Chem.* **1996**, *100*, 6107−6110.
(41) Wellendorff, J.; Lundgaard, K. T.; Mogelhoj, A.; Petzold, V.; Landis, D. D.; Norskov, J. K.; Bligaard, T.; Jacobsen, K. W. Density functionals for surface science: Exchange-correlation model development with Bayesian error estimation. *Phys. Rev. B: Condens. Matter Mater. Phys.* **2012**, *85*, 235149.
(42) Studt, F.; Abild-Pedersen, F.; Varley, J. B.; Nørskov, J. K. CO and CO_2 hydrogenation to methanol calculated using the BEEF-vdW functional. *Catal. Lett.* **2013**, *143*, 71−73.
(43) Catapan, R. C.; Oliveira, A. A. M.; Chen, Y.; Vlachos, D. G. DFT study of the water−gas shift reaction and coke formation on Ni(111) and Ni(211) surfaces. *J. Phys. Chem. C* **2012**, *116*, 20281−20291.
(44) Chen, Y.; Vlachos, D. G. Density functional theory study of methane oxidation and reforming on Pt(111) and Pt(211). *Ind. Eng. Chem. Res.* **2012**, *51*, 12244−12252.
(45) Niu, J.; Guo, F.; Ran, J.; Qi, W.; Yang, Z. Methane dry (CO_2) reforming to syngas (H_2/CO) in catalytic process: From experimental study and DFT calculations. *Int. J. Hydrogen Energy* **2020**, *45*, 30267−30287.
(46) Henkelman, G.; Jónsson, H. A dimer method for finding saddle points on high dimensional potential surfaces using only first derivatives. *J. Chem. Phys.* **1999**, *111*, 7010−7022.
(47) Wan, J.; Fang, G.; Yin, H.; Liu, X.; Liu, D.; Zhao, M.; Ke, W.; Tao, H.; Tang, Z. Pt−Ni alloy nanoparticles as superior counter electrodes for dye-sensitized solar cells: Experimental and theoretical understanding. *Adv. Mater.* **2014**, *26*, 8101−8106.
(48) Akbari, E.; Alavi, S. M.; Rezaei, M. Synthesis gas production over highly active and stable nanostructured Ni-MgO-Al_2O_3 catalysts in dry reforming of methane: Effects of Ni contents. *Fuel* **2017**, *194*, 171−179.
(49) Leofanti, G.; Padovan, M.; Tozzola, G.; Venturelli, B. Surface area and pore texture of catalysts. *Catal. Today* **1998**, *41*, 207−219.
(50) Bus, E.; van Bokhoven, J. A. Hydrogen chemisorption on supported platinum, gold, and platinum−gold-alloy catalysts. *Phys. Chem. Chem. Phys.* **2007**, *9*, 2894−2902.
(51) Singha, R. K.; Shukla, A.; Sandupatla, A.; Deo, G.; Bal, R. Synthesis and catalytic activity of a Pd doped Ni−MgO catalyst for dry reforming of methane. *J. Mater. Chem. A* **2017**, *5*, 15688−15699.
(52) Serrano-Lotina, A.; Rodríguez, L.; Muñoz, G.; Daza, L. Biogas reforming on La-promoted NiMgAl catalysts derived from hydrotalcite-like precursors. *J. Power Sources* **2011**, *196*, 4404−4410.
(53) Hu, Y. H. Solid-solution catalysts for CO_2 reforming of methane. *Catal. Today* **2009**, *148*, 206−211.
(54) Li, J.; Tian, W. P.; Wang, X.; Shi, L. Nickel and nickel−platinum as active and selective catalyst for the maleic anhydride hydrogenation to succinic anhydride. *Chem. Eng. J.* **2011**, *175*, 417−422.
(55) Yu, X.; Zhang, F.; Wang, N.; Hao, S.; Chu, W. Plasma-treated bimetallic Ni−Pt catalysts derived from hydrotalcites for the carbon dioxide reforming of methane. *Catal. Lett.* **2014**, *144*, 293−300.
(56) Dam, A. H.; Wang, H.; Dehghan-Niri, R.; Yu, X.; Walmsley, J. C.; Holmen, A.; Yang, J.; Chen, D. Methane activation on bimetallic catalysts: Properties and functions of surface Ni−Ag alloy. *ChemCatChem* **2019**, *11*, 3401−3412.
(57) Li, X.; Xin, M.; Guo, S.; Cai, T.; Du, D.; Xing, W.; Zhao, L.; Guo, W.; Xue, Q.; Yan, Z. Insight of synergistic effect of different active metal ions in layered double hydroxides on their electrochemical behaviors. *Electrochim. Acta* **2017**, *253*, 302−310.
(58) Li, B.; Li, C.; Cai, J.; Zhao, J. Retracted Article In situ nano-coating on Li1.2Mn0.52Ni0.13Co0.13O2 with a layered@ spinel@ coating layer heterostructure for lithium-ion batteries. *J. Mater. Chem. A* **2015**, *3*, 21290−21297.
(59) Spahr, M. E.; Novák, P.; Schnyder, B.; Haas, O.; Nesper, R. Characterization of layered lithium nickel manganese oxides synthesized by a novel oxidative coprecipitation method and their electrochemical performance as lithium insertion electrode materials. *J. Electrochem. Soc.* **1998**, *145*, 1113−1121.
(60) Zhu, X.; Zhang, Y.-p.; Liu, C.-j. CO adsorbed infrared spectroscopy study of Ni/Al_2O_3 Catalyst for CO_2 reforming of methane. *Catal. Lett.* **2007**, *118*, 306−312.
(61) Xie, Z.; Yan, B.; Lee, J. H.; Wu, Q.; Li, X.; Zhao, B.; Su, D.; Zhang, L.; Chen, J. G. Effects of oxide supports on the CO_2 reforming of ethane over Pt-Ni bimetallic catalysts. *Appl. Catal., B* **2019**, *245*, 376−388.
(62) Mirodatos, C.; Praliaud, H.; Primet, M. Deactivation of nickel-based catalysts during CO methanation and disproportionation. *J. Catal.* **1987**, *107*, 275−287.
(63) Blackmond, D.; Ko, E. Structural sensitivity of CO adsorption and H_2CO coadsorption on $NiSiO_2$ catalysts. *J. Catal.* **1985**, *96*, 210−221.
(64) Agnelli, M.; Swaan, H. M.; Marquez-Alvarez, C.; Martin, G. A.; Mirodatos, C. CO Hydrogenation on a Nickel Catalyst. *J. Catal.* **1998**, *175*, 117−128.
(65) Deng, L.; Miura, H.; Shishido, T.; Hosokawa, S.; Teramura, K.; Tanaka, T. Strong metal-support interaction between Pt and SiO_2 following high-temperature reduction: a catalytic interface for propane dehydrogenation. *Catal. Commun.* **2017**, *53*, 6937−6940.
(66) Vignatti, C.; Avila, M. S.; Apesteguía, C. R.; Garetto, T. F. Catalytic and DRIFTS study of the WGS reaction on Pt-based catalysts. *Int. J. Hydrogen Energy* **2010**, *35*, 7302−7312.
(67) Chen, D.; Lødeng, R.; Svendsen, H.; Holmen, A. Hierarchical multiscale modeling of methane steam reforming reactions. *Ind. Eng. Chem. Res.* **2011**, *50*, 2600−2612.
(68) Tu, W.; Ghoussoub, M.; Singh, C. V.; Chin, Y.-H. C. Consequences of surface oxophilicity of Ni, Ni-Co, and Co clusters on methane activation. *J. Am. Chem. Soc.* **2017**, *139*, 6928−6945.
(69) Aparicio, L. M. Transient isotopic studies and microkinetic modeling of methane reforming over nickel catalysts. *J. Catal.* **1997**, *165*, 262−274.
(70) Wei, J. M.; Iglesia, E. Isotopic and kinetic assessment of the mechanism of reactions of CH_4 with CO_2 or H_2O to form synthesis gas and carbon on nickel catalysts. *J. Catal.* **2004**, *224*, 370−383.

https://dx.doi.org/10.1021/acscatal.0c04429
ACS Catal. 2021, 11, 2398−2411